Synthesis, Structure and Properties of Nickel-Iron-Tungsten Alloy Electrodeposits
PART I: Effect of Synthesis Parameters on Chemical Composition, Microstructure and Morphology

N. Ćirović[1*)], P. Spasojević[1,3], L. Ribić-Zelenović[2*], P. Mašković[2], M. Spasojević[2]
[1]Faculty of Technology and Metallurgy, University of Belgrade, Belgrade, Serbia
[2]Faculty of Agronomy, Čačak, University of Kragujevac, Čačak, Serbia
[3]Joint Laboratory for Advanced Materials of SASA, Section for Amorphous Systems, Faculty of Technical Sciences, University of Kragujevac, Čačak, Serbia

Abstract:

Kinetic and operational electrolysis parameters determine the polarization characteristics, electrodeposition current efficiency, morphology, chemical composition and microstructure of nickel/iron/tungsten alloy deposits. The alloys electrodeposited at a current density of 50 mAcm^{-2} to 1000 mAcm^{-2} contain an amorphous phase and nanocrystals of an FCC solid solution of iron and tungsten in nickel. During annealing at temperatures above 500ºC, amorphous phase crystallization, crystalline grain growth of the FCC phase and a reduction in both internal microstrain and minimum density of chaotically distributed dislocations take place in the alloy. Milling the spongy deposit of the alloy causes amorphous phase crystallization, FCC-phase crystalline grain growth, and size reduction and rounding of powder particles.
Keywords: *Nanostructured alloy, FCC phase, Electrochemical deposition, Milling, Annealing.*

1. Introduction

Nanostructured materials find wide applications in advanced technologies due to their specific properties [1]. Nanocrystalline nickel-iron-tungsten alloys have good electrical, magnetic and mechanical properties, high thermal stability and high corrosion resistance [2-11], and hence their use for a wide range of industrial applications, mostly as materials for microelectronics and microelectromechanical systems. In the electrochemical industry, they serve as cathodes for hydrogen evolution. Nickel-iron-tungsten alloy coatings are hard and smooth, have nice appearance and provide good adherence to steel substrates 2,5,10-13].

The metallurgical fabrication of nickel-iron-tungsten alloys is very expensive due to high energy consumption. More recently, these alloys have been obtained by electrochemical methods from environmentally friendly citrate ammonia solutions without any environmental and health risks [2,5,10-13]. The electrochemical process can result in alloys featuring different phase structures and morphology and different mechanical, electrical, catalytic and corrosion properties, although their chemical composition is the same as that of

---

*) **Corresponding author**: cirovicm@ptt.rs

metallurgically prepared alloys. The properties of electrochemically generated alloys are dependent on solution composition and temperature, deposition current density and electrolyte recirculation rate [14-17]. Tungsten and molybdenum can be electrocodeposited only with iron-group metals [2,18-20]. The mechanism of codeposition of these metals has been investigated in a number of studies [12,16-24]. The effect of kinetic and operational parameters of electrolysis on the chemical composition, microstructure and physicochemical properties of these alloys has been analyzed [2,4,13].

Based on the theory of catalytic reduction, M. L. Holt and L. E. Voaler [25] concluded that coatings are formed by means of successive deposition of thin alternate layers of iron-group metals and tungsten.

O. Younes et al. [22,23] assumed that an electroactive mixed-metal complex consisting of ions of iron group-metals and tungsten is formed in the solution or on the electrode surface. However, the presence of these ions in the solution has not been proven.

E. Chassaing et al. [21] assumed that molybdate and tungstate are reduced at the cathode to lower valence oxides, which are further reduced by adatoms of the iron-group metals.

E. J. Podlaha et al. [18] studied the effect of electrolysis parameters on molybdenum/iron-group metal alloy deposition from citrate electrolytes. They proposed a mechanism based on the adsorption and catalytic reduction of molybdate species. As determined, the species [Me(II)H Cit]$^-$ catalyzes the reduction of molybdates forming an adsorbed reaction intermediate [Me(II)HCit-MoO$_2$]ads (where HCit denotes triply deprotonated citric acid, $C_6H_5O_7^{3-}$, and Me stands for iron-group metals). According to the mechanism proposed, molybdenum can be deposited only if iron-group metal ions are found in the solution, while the reduction of Me^{2+} ions follows an independent path [18].

According to the mechanism proposed by M. D. Obradović et al. [24], during nickel-tungsten alloy deposition from an ammonia-citrate bath, two parallel reactions occur viz. nickel deposition from ammonia-citrate complexes and the reduction of the protonated tungstate-citrate complex with more than one proton to lower valence oxides. Nickel adatoms, resulting from Ni^{2+} reduction, diffuse along the cathode surface until their incorporation into the crystal lattice. During the diffusion, some of these adatoms of Ni$^{\circ}$ collide with the low valence tungstate citrate complex and reduce it to metal tungsten.

The authors [24] have concluded that the chemical composition, phase structure and morphology of nickel-tungsten alloy deposit are dependent on the relationship between the parallel metal codeposition reactions, whereas hydrogen evolution affects only alloy morphology and current efficiency.

F. He et al. [5] have deposited nickel-iron-tungsten coatings with a tungsten content of 18 wt.%, 35 wt.% and 55 wt.% from a solution containing iron sulfate, nickel sulfate, sodium tungstate, citric acid and boric acid. The coatings were smooth, of nice appearance, and adhered well to iron and steel. As-plated coatings with 18 wt.% tungsten are crystalline, with face centered cubic structure of nickel, while those with 35 wt.% and 55 wt.% tungsten are amorphous. After heat treatment at different temperatures, phases such as γ-(Fe, Ni), γ-(Fe, Ni, Fe), β − (Fe, Ni, W), Fe$_6$W$_6$C and Fe$_3$W$_3$C are separated out in succession. Fe-Ni-W alloy coatings with 55 wt.% tungsten, after heat treatment at proper temperatures, appear to have excellent wear resistance and hardness. The deposits with 18 wt.% tungsten are very corrosion resistant and show the best appearances. However, the alloys with 35 wt.% tungsten exhibit superior overall performance.

At current densities between 35 mA cm^{-2} and 70 mA cm^{-2}, M. Donten et al. [2] electrodeposited thin, smooth, hard, well-adhesive amorphous coatings of Ni, Fe, W alloy on iron and copper cathodes from the solution containing NiSO$_4$, FeSO$_4$, Na$_2$WO$_4$, Na$_2$Cit, H$_3$PO$_4$, H$_3$BO$_3$, butynediol and detergent. Pulse electroplating gave smoother and more uniform deposits containing up to 35 mol.%W. The hardness of the alloy increased with increasing tungsten content.

J. Ahmad et al. [26] used anammoniacal citrate bath containing $NiSO_4$, $FeSO_4$ and Na_2WO_4, and produced nanostructured Fe-Ni-W alloys at low current densities, and amorphous alloys at high current densities. They found that as the current density increases, tungsten content increases while iron content decreases. The hardness of the alloys increases with increasing tungsten content. The best mechanical properties are exhibited by $Ni_{51}Fe_{29}W_{20}$ alloy obtained at a current density of 60 mAcm^{-2}. Addition of hypophosphite to the solution causes a decrease in W and Fe contents and an increase in P and Ni contents in the alloy.

K. R. Sriraman et al. [3,4] obtained smooth coatings on cathodes made of copper and low-carbon and low-alloy steels from the solution containing $NiSO_4$, $FeSO_4$, Na_2WO_4, $Na_3C_6H_5O_7 \cdot$ 2 H_2O (trisodium citrate dihydrate), NH_4Cl, H_3BO_3, NaBr, $COC_6H_4SO_2N$ Na $\cdot 2$ H_2O (sodium saccharin), $CH_3(CH_2)_{10}CH_2OSO_3Na$ (sodium lauryl sulphate). Increasing the deposition current density from 50 mAcm^{-2} to 200 mAcm^{-2} in the alloy leads to an increase in the contents of W (from 0.22 mol.% to 10.39 mol.%) and Fe (from 15.8 mol.% to 24.58 mol.%), and a decrease in Ni content with crystal grain size of 15 nm to 2 nm of the FCC-structured solid solution of W and Fe in Ni. The corrosion resistance of the alloys increases with W content up to 9.20 mol.% and then decreases.

P. Esther et al. [6] used the solution containing $NiSO_4$, $FeSO_4$, Na_2WO_4, citric acid and diammonium citrate, and produced smooth, crack-free, nanocrystalline Ni-Fe-W coatings with good adherence to the substrate (copper and stainless steel), which are granular in nature. An increase in citrate concentration in the solution causes a decrease in Ni content and an increase in W content of the coatings. All alloys ($Ni_{67.5}Fe_{25.5}W_{7.0}$; $Ni_{61.2}Fe_{24.5}W_{14.3}$; $Ni_{54.5}Fe_{27.3}W_{18.2}$) contained a solid solution of Fe and W in Ni with FCC-structured nanocrystals. As W content in the alloy increases (from 7.0 wt.% to 18.2 wt.%), crystal size decreases (from 38.7 nm to 24.6 nm), while strain increases (from $5 \cdot 10^{-4}$ to $10 \cdot 10^{-4}$). Coatings with 14 wt.% W exhibit the best soft magnetic properties of high saturation magnetic flux density B_S=0.99T and coercivity Hc = 8 Oe. As W content increases, the saturation magnetic flux density decreases, but coercivity increases.

M. Banerjee et al. [7] found that Ni-Fe-W alloys with a high content of Ni (≥ 80 mol.%) and Fe content below 7 mol.% have a low Curie temperature (Tc ≤ 190 K).

S. J. Mun et al. [12] obtained smooth coatings of Ni-Fe-W alloy on carbon steel substrate from the solution containingNa_2WO_4, $NiSO_4$, $FeSO_4$, sodium citrate, NH_4Cl, 2-butane-1.4-diol and sodium lauryl, at a current density of 60 mAcm^{-2}. Increasing Fe^{2+} ion concentration (from 0.01 mol dm^{-3} to 0.07 mol dm^{-3}) results in an increase in the contents of Fe (from 2.5 mol.% to 8.7 mol.%) and W (from 9.5 mol.% to 14 mol.%) in the alloy. The surface cracks were diminished with increasing iron content in the alloy. The addition of 8 mol.% iron to the alloy completely removed the surface microcracks. The hardness of the coatings increases moderately with increasing W content. XPS study results showed that the matrix formed by the FCC-structured solid solution of tungsten and iron in nickel contained $NiWO_4$ nanocrystals. Heat treatment remarkably improved the hardness of the alloys, especially at 500 $^{\circ}$C, due to precipitation hardening and nanosized grains of $NiWO_4$. At temperatures above 500 $^{\circ}$C, hardness decreases significantly with increasing annealing temperature due to increased crystallite size.

Amorphous and nanocrystalline alloys occur in a metasTab. state. Annealing at elevated temperatures and milling change their microstructure and morphology, thus affecting their mechanical, electrical and magnetic properties, catalytic activity, corrosion resistance and thermal stability [27,28]. Annealing at temperatures lower than crystallization temperature leads to structural relaxation of the alloy involving short-range ordering, resulting in increased electronic density of states in the conduction band near the Fermi level and increased mean length of the free electron path [27,28].Amorphous phase crystallization and nanocrystal growth occur at higher temperatures and lead to changes in the physical properties and chemical behavior of the alloys [27,28].

The objective of this study was to present a review of research conducted as part of the Project Ref. No. 172057 financially supported by the Ministry of Education and Science of the Republic of Serbia on the effect of electrodeposition parameters, milling and annealing temperature on the chemical composition, microstructure and morphology of nickel-iron-tungsten alloy deposits (Part I) and determine the effect of these features on their magnetic properties and hardness (Part II).

2. Experimental

The electrochemical deposition of nickel-iron-tungsten alloy was performed in a glass cell of 2 dm^3 volume. A 12 cm^2 Pt plate served as the anode. Titanium, mild steel and copper plates were used as the cathodes. The titanium cathode was 4.5 cm^2, and mild steel and copper cathodes were each 2 cm^2 in surface area. Cathode thickness was 3 mm. The cathodes were positioned parallel to the anode at a distance of 0.5 cm. The cell had a saturated calomel electrode placed in a separate compartment connected by Luggin capillary to the working electrode. The cell was placed in a thermostat. The operating temperature ranged from 50 ºC to 70 ºC. During the measurement, a standard electrical circuit, composed of a programmer equipped with a potentiostat (Potentiostat/Galvanostat Model 173, EG G Princeton Applied Research, Princeton, USA), an X-Y recorder (Hewlett Packard 7035B) and a digital voltmeter, was used.

Solutions A and B of the following compositions were used:

	$NiSO_4 \cdot 6H_2O$	$FeSO_4$	$Na_2WO_4 \cdot 2H_2O$	$Na_3C_6H_5O_7 \cdot 2H_2O$	NH_4Cl	Na_2SO_4	H_3BO_3	$NaBr$
Solution A, mol dm^{-3}	0.2	0.02	0.004	0.24	0.8	0.3	/	/
Solution B, mol dm^{-3}	0.012	0.004	0.01	0.06	0.5	/	1.0	0.15

The pH of solution A was 9.2±0.1, while pH of solution B was 9.2±0.1. The temperature of solution was 65±0.5 ºC, while for solution B were 50±0.5ºC; 60±0.5ºC and 70±0.5 ºC. The pH value of the solution during the electrolysis was maintained by addition of ammonia solution. The solutions were prepared with p.a. chemicals (Merck) and triply distilled water.

The alloys were deposited galvanostatically at current densities ranging from 40 mA cm^{-2} to 1000 mA cm^{-2}. The potentials presented in this paper were corrected for the ohmic voltage drop determined by the galvanostatic pulse method and referenced to the standard hydrogen electrode. The current efficiency of alloy deposition was the result of measurement of alloy deposit weight and hydrogen evolution rate. The time required to fill a graduated burette located above the working electrode with hydrogen was measured. The thickness of the coatings was 20 μm. Upon electrolysis, to prevent oxidation, the resulting alloys were washed three times with water and 0.1 wt.% benzoic acid solution and then dried at 105 ºC. Scanning electron microscopy (SEM) analysis was performed on a JEOL-JSM 5300 equipped with an EDS-QX 3000 spectrometer. The chemical composition of the alloy was determined by energy dispersive X-ray spectroscopy (EDS) using attachment to SEM as well as by atomic absorption (PEKTAR-A 200-VARIAN). X-ray diffraction (XRD) was recorded on a Philips PW 1710 diffractometer using CuK_α radiation (λ = 0.154 nm) and a graphite monochromator. XRD data were collected with a step mode of 0.03º and a collection time of 1.5 s $step^{-1}$. The analysis of the size and shape of powder particles was performed using a Leica Q500 MC automatic device for microstructural analysis. The as-prepared alloy was milled in an alcohol medium using a Planetary Ball Mill Type PM 400.

3. Results and discussion

Nickel-iron-tungsten alloy deposits were obtained from an ammonia citrate solution of nickel and iron sulfates and sodium tungstate on titanium, mild steel and copper cathodes. The chemical composition, morphology, microstructure and physicochemical properties of the deposits are dependent on bath composition and temperature, electrodeposition current density and the nature of the cathode. The chemical composition of the deposit was determined by atomic absorption and electronic dispersion spectroscopy (EDS). Based on six measurements by each method, the average composition was determined. The chemical composition did not depend on the nature of the cathode. In the current density range of 50 mA cm^{-2} to 300 mA cm^{-2}, the deposit composition is dependent on deposition current density. At higher current densities, ranging from 300 mA cm^{-2} to 1000 mA cm^{-2}, the composition is not dependent on current density (Fig. 1).
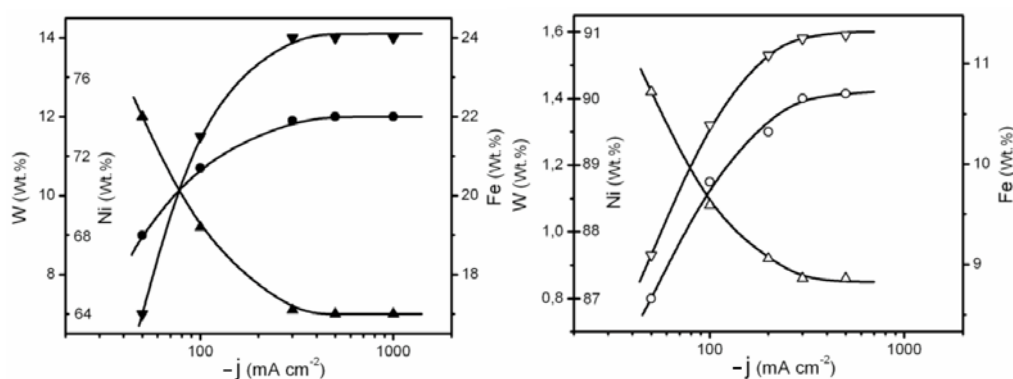
Fig. 1. Dependence of deposit composition on deposition current density; ▲, △-Ni; ▼,

-Fe; ●,○ W; ▲,▼,● deposit product from solution B; ▽,△,○- deposits produced from

solution A.

In the current density range of 50 to 300 mA cm^{-2}, as the deposition current density increases, iron and tungsten contents increase and nickel content decreases.

In the EDS spectra of nickel-iron-tungsten alloy deposits, weakly pronounced peaks of oxygen are observed (Fig. 2 a). Oxygen is most likely present on the surface in metal oxide or hydroxide form [29]. M. Donter [29] showed that a smooth surface oxide layer is formed by the oxidation of the metals with atmospheric oxygen. During the 30-minute annealing (of the coating) at 700 ºC, the surface of the coating is additionally oxidized, and hence the considerably higher oxygen peak in the EDS spectrum (Fig. 2 b). When determining the average composition of the alloy, the oxygen content was not considered.

The composition of the alloys at high current densities is not dependent on current density since the codeposition of all three metals takes place under slow diffusion of reactive species. The electrodeposition of nickel-iron-tungsten alloy is a complex process due to simultaneous reactions taking place on the cathode: a) hydrogen evolution; b) tungstate reduction to lower valence oxides; c) nickel deposition; d) iron deposition, and e) reduction of lower valence tungsten oxides to elementary tungsten. The nature of the species present in the electrolyte solution determines the mechanism and kinetics of alloy deposition and, hence, the chemical composition, phase structure and morphology of the alloy.

In solutions A and B, electrochemically inactive WO_4^{2-} ions form the complex $[WO_4HCitH_x]^{5-x}$ (x = 0; 1; 2 and 3) with citrate ions. At 9 < pH < 10, the dominant species in the solution are $[WO_4HCitH]^{4-}$ and $[WO_4HCit]^{5-}$ [24]. The concentration of the citrate-tungstate complex containing more than one proton is extremely low. On the cathode, only

citrate-tungstate complexes containing two and more protons are reduced to lower valence tungsten oxides [24].
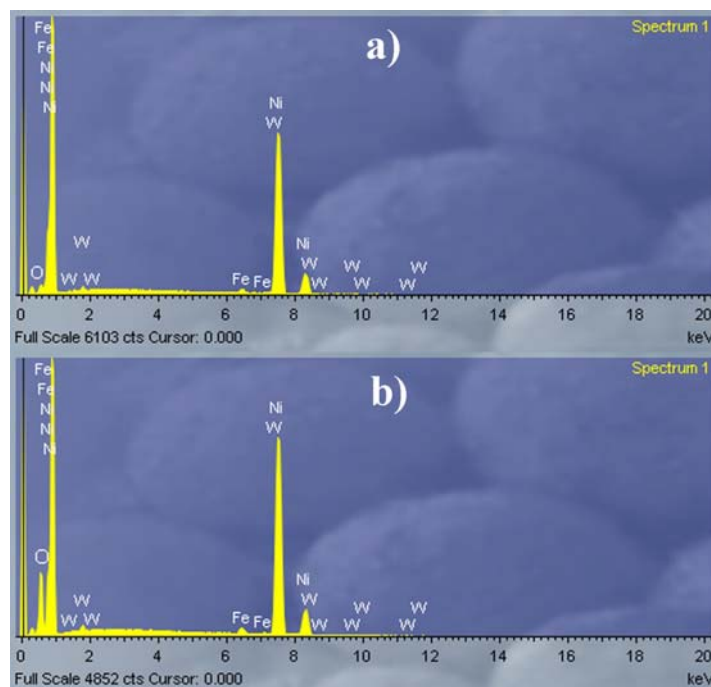

Fig. 2. EDS spectrum of the nickel-iron-tungsten alloy deposit on a mild steel cathode electrodeposited from solution A at 50 mAcm-2. a) – as-deposited coating; b) – coating annealed for 30 minutes at 700ºC.

In the ammonium citrate solution, iron and nickel ions (Me) build complex ions $[Me(HCit)(NH_3)_x(H_2O)_y(OH)_z]$ $(x + y + z = 3)$ [24]. The ammonium ions NH_4^+ play a triple role in nickel-iron-tungsten alloy deposition: a) enable maintenance of a suiTab. pH of the solution, b) donate protons for the formation of electroactive citrate-tungstate complexes, and c) form electroactive complexes with iron-group metal ions. No mixed-metal citrate complexes of ions of iron-group metals and tungstate are formed in the solution [24]. At current densities above 500 mAcm^{-2}, the reduction of the citrate-tungstate complex with two and more protons to lower valence tungsten oxides is a diffusion controlled process. Under diffusion control conditions, other parallel reactions viz. nickel deposition and iron deposition occur. The exchange of charges of these ions takes place in two steps [22,24,30]. The first step involves the formation of very unsTab. intermediates Ni^+ and Fe^+ that exist on the electrode surface as adions. In the second step, Ni^o and Fe^o adions are formed, and they diffuse along the cathode surface until their incorporation into the crystal lattice. Ni^o and Fe^o adatoms are stronger reductants, and their surface concentrations are higher than those of Ni^+ and Fe^+ adatoms, and hence the greater likelihood for them to collide with lower valence oxides of tungsten during surface diffusion and reduce them to metal tungsten [24]. At higher current densities, $j > 500$ mA cm^{-3}, the diffusion of electroactive species from the bulk solution to the cathode surface is the rate-determining step for nickel-iron-tungsten alloy deposition. Therefore, at $j > 500$ mA cm^{-2}, the surface concentrations of Ni^o, Fe^o and lower valence tungsten oxide, the surface diffusion rate of Ni^o and Fe^o and the rate of reduction of lower valence tungsten oxide are independent of current density. The conclusions presented in this paper provide an explanation of why the chemical composition and phase structure of the

deposits obtained in the current density range of 500 mA cm^{-2} < j < 1000 mA cm^{-2} do not depend on current density. However, increasing current density leads to an increase in both cathode polarization and hydrogen evolution rate. As the polarization increases, the critical diameter of the nucleus decreases, thus causing the formation of smaller crystals and change in the deposit morphology. The hydrogen evolution rate also affects the morphology of the deposit and the shape of particle size distribution of powders.

The effect of the solution temperature on the composition of the electrodeposited nickel-iron-tungsten alloy is presented in Fig. 1. Under diffusion-controlled deposition conditions, the chemical composition of the alloy is not significantly affected by the solution temperature in the temperature range 50 ºC < t < 70 ºC. This indicates that the diffusion coefficients for all three electroactive species increase at approximately the same rate with increasing temperature of the solution.
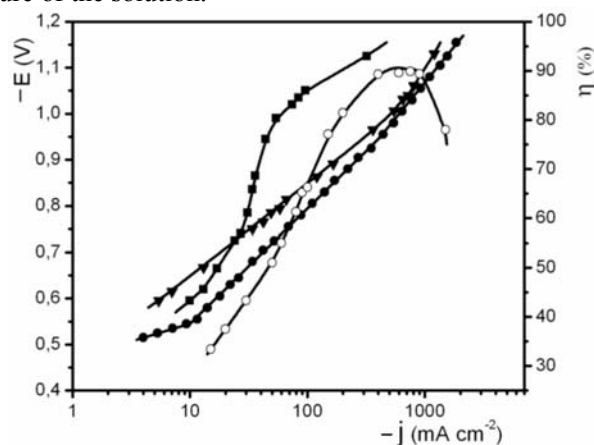
Fig. 3. Polarization curves: ● - polarization curve for the total cathodic process; ▼ - polarization curve for nickel-iron-tungsten alloy deposition, ■ - polarization curve for hydrogen evolution, and ○ - dependence of current efficiency of the alloy during deposition from solution A.

Polarization curves were recorded and current efficiency of the alloy was determined. First, on the titanium cathode, a spongy Ni$_{87.3}$Fe$_{11.3}$W$_{1.4}$ alloy deposit of high real area was produced by 30-minute electrodeposition from solution A at a current density of 500 mA cm^{-2}. Then, the cathode polarization curve was recorded by the potentiostatic method. The values of the current were registered for 30 seconds after the potential had been reached (Fig. 3).

The high Tafel slope of the total cathodic polarization curve of 320 mV in the current density range of 10 mA cm^{-2} to 400 mA cm^{-2} indicates the presence of a poorly conductive oxide film on the deposit surface.

The current efficiency of the alloy increases with increasing current density up to 500 mA cm^{-2}. Then, further increase in current density up to 900 mA cm^{-2} does not have a significant effect on current efficiency. At current densities above 900 mA cm^{-2}, current efficiency decreases with increasing current density. The total cathodic polarization curve and current efficiency values were used to determine the polarization curves for alloy deposition and hydrogen evolution (Fig. 3). In the current density range of 5 mA cm^{-2} to 300 mA cm^{-2}, there exists a linear dependence of the logarithm of deposition current density on the potential. At higher current densities, linear dependence disappears since activation-controlled deposition is transformed into a diffusion-controlled process [10]. The limiting diffusion current is high due to the high real area of the spongy deposit.

The rate of hydrogen evolution increases up to − 760 mV. In the potential range of − 760 mV to -960 mV, there exists a limiting diffusion current [10]. At potentials more negative

than -960 mV, the hydrogen evolution rate follows Tafel's dependence with a slope of 130 mV. At potentials more positive than -960 mV, hydrogen is evolved from NH_4^+ and $(HCit)^{3-}$ ions, and at potentials more negative than -960 mV, the dominant reaction is hydrogen evolution through water reduction [10]. The phase structure of the alloys was identified using an X-ray analysis. X-ray diffractograms were recorded for different compositions of the alloys obtained at different current densities and on cathodes formed of different materials. The position, shape and width of the peaks are dependent on alloy composition and current density, and do not depend on the nature of the cathode material.
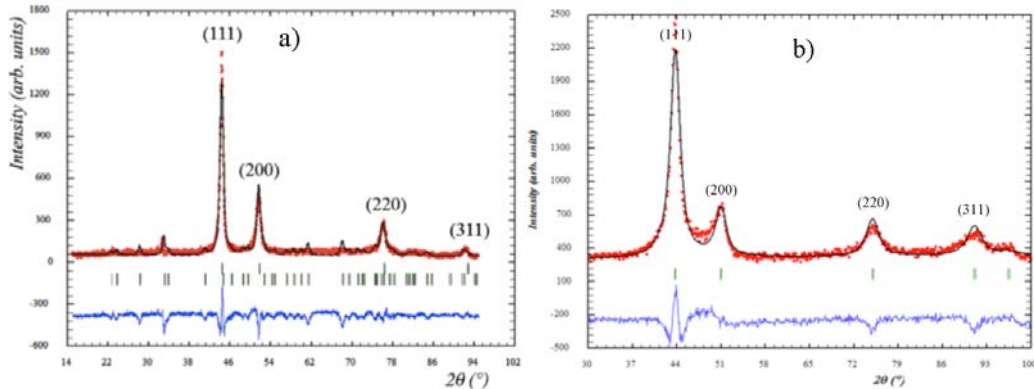
Fig. 4. Rietveld diagrams of as-deposited alloys: a) – $Ni_{87.3}Fe_{11.3}W_{1.4}$ from solution A at 500 mA cm^{-2} and b) – $Ni_{65}Fe_{24}W_{11}$ from solution B at 65 ºC and at 500 mA cm^{-2}. P4/nmm space group structure [8,9].

Fig. 4. presents X-ray diffractograms of as-produced nickel-iron-tungsten alloys obtained from solution A and solution B. The dots represent measured values. The upper solid line stands for calculated values for the structural model. The difference between measured and calculated values is represented by the bottom solid line. The vertical dashes denote positions of Bragg's reflections; the upper dashes represent the positions of peaks for the FCC phase of the solid solution of Fe and W in Ni, while the bottom dashes denote the position of peaks for the WO_3 structure in the P4/nmm space group structure [8,9]. [8,9].

The X-ray diffraction patterns of as-produced deposits obtained from solutions A and B at current densities between 50 mA cm^{-2} and 1000 mA cm^{-2} show only distinct peaks for (111), (200), (220) and (311) planes of the FCC phase of the solid solution of iron and tungsten in nickel. There are no distinct peaks for the crystal phase of WO_3. No peaks are observed for intermetallic compounds. The presence of the FCC phase of the solid solution in the electrochemically produced nickel-iron-tungsten alloys at tungsten contents lower than 18 wt.% was also determined elsewhere [2,5,7-9,27].

The X-ray diffraction patterns of as-produced alloys deposited under the same conditions on cathodes made of different materials (copper, mild steel, titanium) are analogous. This indicates that the nature of the cathode material does not affect the phase structure of the deposit.

The deposition current density affects the nature of the deposit phase structure. As the current density increases, the peak intensity decreases and the half-height width increases, thus indicating that small-sized crystals are formed at elevated current densities (Tab. I; Fig. 5). Current density has both a direct and an indirect effect on mean crystal size [14]. The direct effect is due to the increase in cathodic polarization occurring due to increasing current density. The increase in polarization decreases the critical nucleus radius and reduces the number of atoms making up the nucleus. The number of atoms in the critical nucleus declines with the square of polarization. This considerably enhances nucleation and causes the

formation of smaller sized crystal grains [14].

Tab. I Values of microstructural parameters for electrodeposited
nickel-iron-tungsten alloys

Alloy composition (wt.%)	$Ni_{90.1}Fe_{9.1}W_{0.8}$	$Ni_{88.45}Fe_{10.4}W_{1.15}$	$Ni_{87.6}Fe_{11.1}W_{1.3}$	$Ni_{87.3}Fe_{11.3}W_{1.4}$
Current density, j, (mA cm^{-2})	50	100	200	300
Solution temperature, t, (ºC)	65	65	65	65
Mean crystal size, D, (nm)	14.0 (3)	10.1 (3)	9.5 (3)	9.2 (3)
Mean microstrain value, ε	$1.5(2)·10^{-3}$	$1.9(4)·10^{-3}$	$2.1(3)·10^{-3}$	$2.3(3)·10^{-3}$
Minimum density of chaotically distributed dislocations, δ, (cm^{-2})	$1.7(3)·10^{12}$	$4.5(3)·10^{12}$	$7.6(3)·10^{12}$	$8.9(4)·10^{12}$
Alloy composition (wt.%)	$Ni_{87.3}Fe_{11.3}W_{1.4}$	$Ni_{65}Fe_{24}W_{11}$	$Ni_{65}Fe_{24}W_{11}$	$Ni_{65}Fe_{24}W_{11}$
Current density, j, (mA cm^{-2})	500	500	1000	1000
Solution temperature, t, (ºC)	65	65	65	50
Mean crystal size, D, (nm)	8.8 (3)	3.4 (3)	3.3 (4)	3.3 (4)
Mean microstrain value, ε	$2.3(3)·10^{-3}$	$4.1(2)·10^{-3}$	$5.1(3)·10^{-3}$	$5.1(3)·10^{-3}$
Minimum density of chaotically distributed dislocations, δ, (cm^{-2})	$8.9(4)·10^{12}$	$2.6(3)·10^{13}$	$2.75(3)·10^{13}$	$2.70(3)·10^{13}$

Current density affects the composition of the deposited alloy, and the composition of the alloy affects its microstructure. Accordingly, indirectly through alloy composition, current density affects the nature of the deposit (Tab. I, Fig. 6).
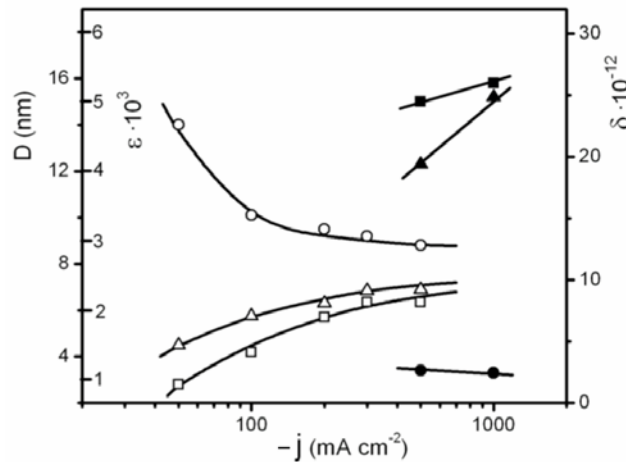
Fig. 5. Mean crystallite size, D, (○; ●), mean microstrain values, ε, (Δ; ▲) and minimum densities of chaotically distributed dislocations, δ, (□; ■) as dependent on deposition current density. ○; Δ; □ - deposits obtained from solution A; ●, ▲, ■- deposits obtained from solution B.
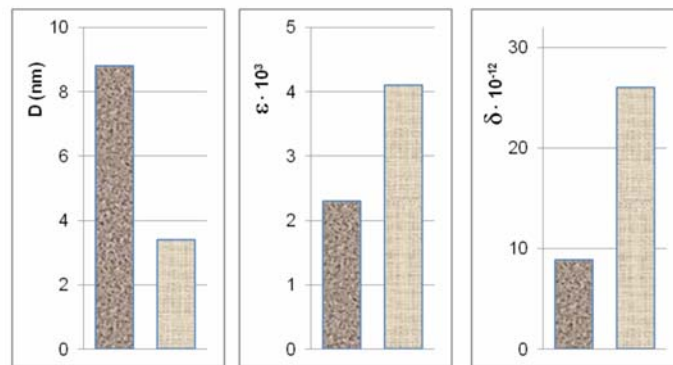
**Fig. 6.** Values of mean crystallite size, D, mean microstrain values, ε, and minimum densities of chaotically distributed dislocations, δ, of the alloys:
▨i$_{87.3}$Fe$_{11.3}$W$_{1.4}$obtained from solution A at 500 mAcm^{-2}, and
▨i$_{65}$Fe$_{24}$W$_{11}$ obtained from solution B at 500 mAcm^{-2} .

Tungsten and iron deform the crystal structure of nickel, thus hindering crystal grain growth [2-6,12,16-32]. In the FCC phase of the solid solution, the atoms of these metals increase the mean interatomic distance, causing peak maxima to shift to lower 2θ values. The relative integral of FCC-phase peak intensity decreases with increasing deposition current density, which indicates that the alloys contain an amorphous phase and that the proportion of the amorphous phase is higher in the deposits with smaller nanocrystals obtained at higher current densities. TEM images show that the nickel-iron-tungsten electrodeposits composed of nanocrystals less than 15 nm in size contain an amorphous matrix as well, and that the proportion of the amorphous phase is higher in deposits having smaller nanocrystals [3,4,31,32]. The increase in deposition current density and the increase in tungsten and iron contents in the solid solution of the FCC phase cause an increase in both mean microstrain values and minimum density of chaotically distributed dislocations (Tab. 1, Figs. 5 and 6). As shown in Tab. I and Fig. 5, the increase in deposition current density from 50 mA cm^{-2} to 200 mA cm^{-2} causes an abrupt decrease in crystallite size and a sudden increase in internal microstrain and minimum density of chaotically distributed dislocations. These abrupt changes are induced by simultaneous increases in current density and tungsten and iron

_____

contents (Fig. 1). At current densities above 200 mA cm^{-2}, tungsten content in the alloy does not change substantially with increasing current density. This results in a slower decrease in mean crystal size and a slower increase in internal microstrain and minimum density of chaotically distributed dislocations. Fig. 6 and Tab. I show that the increase in tungsten content from 1.4 wt.% to 11 wt.% causes a decrease in mean crystallite size from 8.8 nm to 3.4 nm and a relatively high increase in internal microstrains and minimum density of chaotically distributed dislocations. Therefore, nickel-iron-tungsten alloy deposits with a relatively high tungsten content (11 wt.%) obtained at high current densities of 500 mA cm^{-2} to 1000 mA cm^{-2} have a low mean crystallite size (3.4-3.3 nm) of the FCC phase of the solid solution of tungsten and iron in nickel and contain a high amount of amorphous phase.

The solution temperature in the temperature range 50 ºC to 70 ºC has no significant effect on the chemical composition and microstructure of the $Ni_{65}Fe_{24}W_{11}$ electrodeposits obtained at high current densities of 500 mA cm$^{-2} \leq j \leq 1000$ mA cm^{-2} since in this temperature range the diffusion coefficients for the electroactive species of nickel, iron and tungsten increase at approximately the same rate with increasing temperature of the solution. The morphology of the nickel-iron-tungsten alloys electrodeposited from solutions A and B depends on the chemical composition, solution temperature, deposition current density and cathode nature.
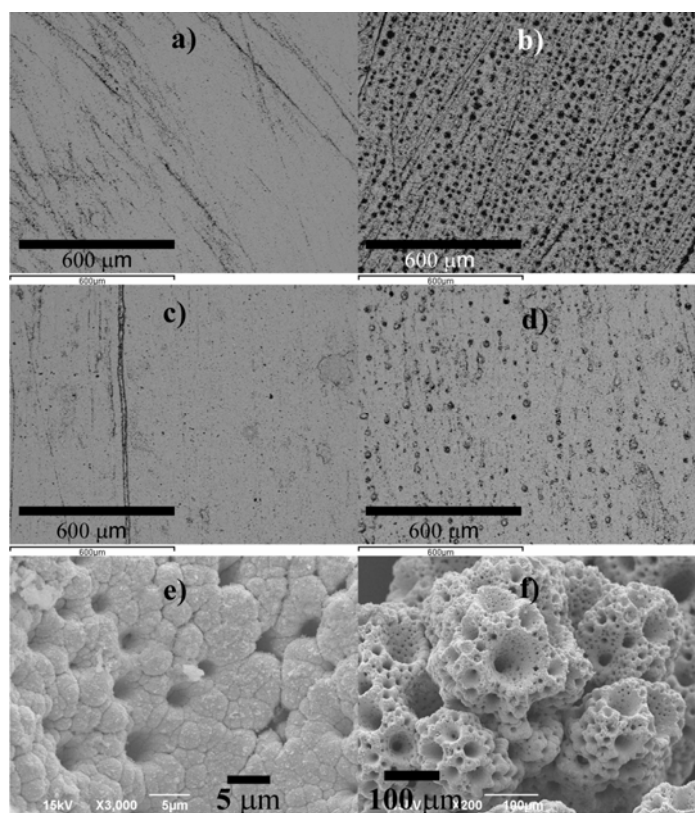

Fig. 7. SEM micrographs of $Ni_{87.3}Fe_{11.3}W_{1.4}$alloy deposited at different current densities on a copper substrate (a, b); on an iron substrate (c, d) and on a titanium substrate (e, f):
a) – 50 mA cm^{-2}; b) – 300 mA cm^{-2}; c)– 200 mA cm^{-2}; d) – 300 mA cm^{-2};
e)– 500 mA cm^{-2}; t = 0.5 h and f)– 1000 mA cm^{-2}; t=1.5 h (h – deposition time in hours).

Electrodeposition from solution A in the current density range of 40 mA cm^{-2} to 300 mA cm^{-2} results in the formation of coatings. At higher current densities (500 mA cm^{-2} to

1000 mA cm^{-2}), coatings exhibiting craters and cracks are formed first, and then a spongy deposit is created as the result of further deposition (Fig. 7 a)-f)). Smooth shiny coatings on copper are formed in the current density range of 40 mA cm^{-2} to 120 mA cm^{-2}, and those on steel in the range of 40 mA cm^{-2} to 220 mA cm^{-2}. At current densities higher than 120 mA cm^{-2} on the copper cathode, and at densities higher than 220 mA cm^{-2} on the steel cathode, rough matte coatings with cracks and craters are formed. The roughness and numbers of cracks and craters increase with increasing deposition current density. The coatings on copper have higher roughness and more cracks and craters. The nature of the cathode material affects the adhesion, internal microstrain value, numbers of cracks and numbers of active centers for hydrogen evolution. The number of craters is dependent on the hydrogen evolution rate. At current densities higher than 500 mA cm^{-2}, a coating consisting of globules with a high number of microcracks and craters is formed on the cathode and is subsequently transformed into a spongy deposit over time (Fig. 7e) and Fig. 7 f)).

Deposition from solution B at current densities between 40 mA cm^{-2} and 300 mA cm^{-2} results in considerably darker rougher coatings with a higher number of cracks compared to coatings deposited from solution A. At higher current densities, powders are deposited (Fig. 8 a)-f)). SEM micrographs show that larger powder particles are mostly cauliflower-shaped and smaller ones are dendritic in shape.
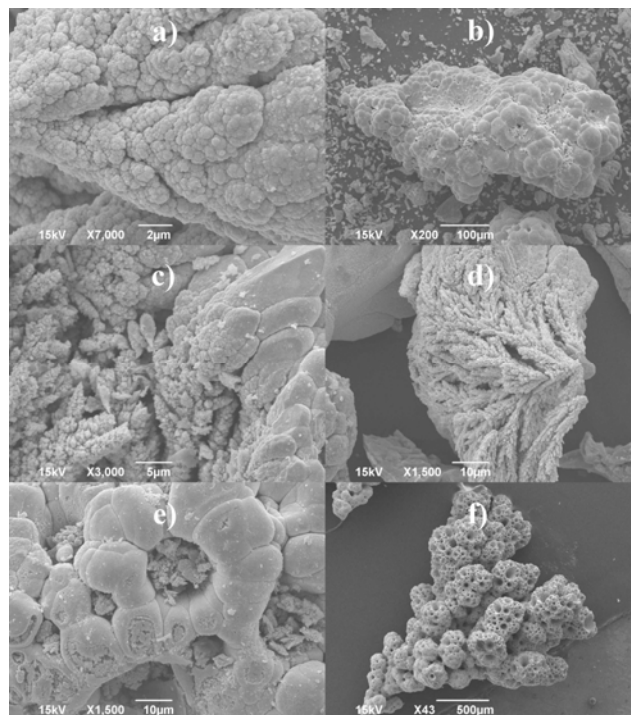
Fig. 8. SEM micrographs of Ni$_{65}$Fe$_{24}$W$_{11}$: a) - cauliflower-like particles (j = 1000 mA cm^{-2}, t = 65 ºC); b) – a cauliflower-shaped particle the surface of which contains tiny dendrite-shaped particles and craters on which hydrogen evolved (j = 500 mA cm^{-2}, t = 65 ºC); c) –on the left side of the micrograph, there are dendrite-shaped particles with a high number of secondary and higher order branches. On the right side of the micrograph, there is a cauliflower shaped particle (j = 500 mA cm^{-2}, t = 65 ºC); d) – a dendrite particle with a large number of branches undergoing transformation into a cauliflower (j = 500 mA cm^{-2}, t = 65 ºC); e) – a cauliflower particle with differently sized craters in which hydrogen has evolved. Dendrite particles are present in the craters (j = 500 mA cm^{-2}, t = 65 ºC), and f) – a sponge-like particle (j = 1000 mA cm^{-2}, t = 65 ºC).

_____

Dendrites have secondary and higher-order branches. The density of branches increases with increasing deposition current density. The cauliflower-shaped particles have craters and their density increases with increasing deposition current density. On the surface of the cauliflower-shaped particles and particularly in craters, dendrites are formed (Fig. 8-e)). Fig. 8-d) presents a SEM micrograph for particles formed as dendrites, which after a certain period of electrolysis undergo transformation into a cauliflower. At high current densities, the strong hydrogen evolution is accompanied by the formation of sponge-shaped particles (Fig. 8-f)).

The size distribution and shape of particles is dependent on deposition current density and solution temperature (Fig. 9). At higher current densities and at a higher solution temperature, smaller-sized particles are formed. The agglomeration of small-sized particles
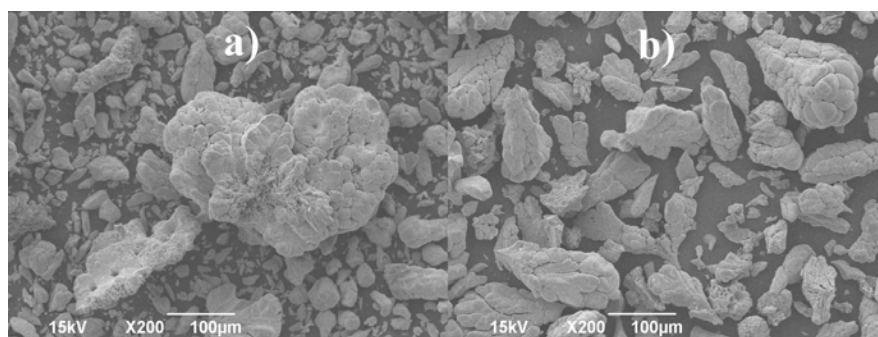
Fig. 9. SEM micrographs of $Ni_{65}Fe_{24}W_{11}$ powders electrodeposited at: a) j = 1000 mA cm^{-2}, t = 65 ºC and b) j = 500 mA cm^{-2}, t = 6 5ºC.

Annealing causes microstructural changes in the nickel-iron-tungsten electrodeposits. The phase changes were identified by X-ray analysis. As-produced deposits were annealed for 60 minutes. Then, they were cooled at 25 ºC, following which X-ray diffractograms were recorded. The X-ray diffractograms of the alloys annealed at 300 ºC and 400 ºC do not significantly differ from those of the as-deposited alloys. As in X-ray diffractograms of as-deposited alloys, the X-ray diffractograms of the alloys annealed at t ≥ 500 ºC have only peaks of the FCC phase of the solid solution of iron and tungsten in nickel. Only the peak intensity is higher, and the half-height width is lower. The position of maxima is shifted to higher values of 2θ. The relative integral of the peak intensity of annealed alloys is higher than that of as-deposited alloys. The difference is higher in alloys obtained at higher current densities. This indicates that as-produced deposits contain an amorphous phase and that its content increases with increasing current density. During annealing at t ≥ 500 ºC, amorphous phase crystallization and crystal grain growth of the FCC phase occur in the alloy parallel to a decrease in internal microstrain value and minimum density of chaotically distributed dislocations (Tab. II).
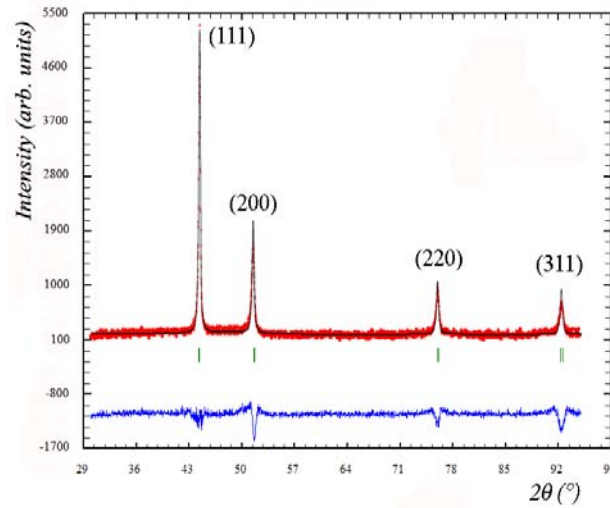
Fig. 10. Rietveld diagrams of $Ni_{87.3}Fe_{11.3}W_{1.4}$ alloy annealed for 60 minutes at 600 ºC and obtained at a current density of 300 mA cm^{-2}. The dots represent measured values. The upper solid line stands for calculated values for the structural model. The difference between measured and calculated values is represented by the bottom solid line. The vertical dashes denote positions of Bragg's reflections for different planes of the FCC phase of the solid solution [9].

Tab. II Values of microstructural parameters for nickel-iron-tungsten alloys annealed for 60 minutes at 600 ºC as dependent on deposition current density [9,10].

Alloy composition (wt.%)	$Ni_{90.1}Fe_{9.1}W_{0.8}$	$Ni_{88.45}Fe_{10.4}W_{1.15}$	$Ni_{87.6}Fe_{11.1}W_{1.3}$	$Ni_{87.3}Fe_{11.3}W_{1.4}$	$Ni_{87.3}Fe_{11.3}W_{1.4}$	$Ni_{65}Fe_{24}W_{11}$
Current density, j, (mA cm^{-2})	50	100	200	300	500	500
Mean crystallite size, D, (nm)	27.3(2)	22.4(3)	23.3(2)	23.2(2)	22.5(2)	17.2(3)
Mean microstrain value, ε	0.1(1)·10^{-3}	0.4(1)·10^{-3}	0.3(1)·10^{-3}	0.3(2)·10^{-3}	0.4(1)·10^{-3}	0.7(1)·10^{-3}
Minimum density of chaotically distributed dislocations, δ, (cm^{-2})	0.06(1)·10^{12}	0.09(3)·10^{12}	0.08(3)·10^{12}	0.08(4)·10^{12}	0.1(3)·10^{12}	0.5(3)·10^{12}

The effect of milling on the microstructure and morphology of the spongy deposit of $Ni_{87.3}Fe_{11.3}W_{1.4}$ alloy was examined. Upon milling of as-deposited samples for 4h; 6h; 8h and 12 h, X-ray diffractograms were recorded. Only FCC-phase peaks were obtained. The increase in milling time causes an increase in peak intensity and a decrease in half-height width. This suggests that milling causes crystal grain growth of the FCC phase and a

simultaneous decrease in both mean microstrain value and minimum density of chaotically distributed dislocations (Tab. III).

Tab. III Values of microstructural parameters for $Ni_{87.3}Fe_{11.3}W_{1.4}$ after eight hours of milling

Current density, j, (mA cm^{-2})	Mean crystallite size, D, (nm)	Mean microstrain value, ε	Minimum density of chaotically distributed dislocations, δ, (cm^{-2})
500	10.6(3)	1.9(4) $\cdot 10^3$	4.3(3)$\cdot 10^{12}$

The longer the milling time, the higher the value of the relative integral of (111), (200) and (311) peak intensities (Tab. 4). This indicates the presence of an amorphous phase in the as-deposited alloy which under goes crystallization during milling. During milling, local overheating occurs in the alloy, causing amorphous phase crystallization, FCC-phase crystal grain growth and a decrease in internal microstrain and minimum densities of chaotically distributed dislocations.

Tab. IV Relative integrals of peak intensities for as-deposited, annealed and milled $Ni_{87.3}Fe_{11.3}W_{1.4}$ alloy obtained from solution A at 500 mAcm^{-2} (The value of the relative integral of peak intensities for the alloy annealed for 60 minutes at 600ºC was taken to be equal to 1).

As-deposited alloy	Alloy annealed for 60 minutes at 600 ºC	Alloy milled for 4 h	Alloy milled for 8h	Alloy milled for 12 h
0.56	1.0	0.85	0.93	0.98

The properties of the powder are dependent on the shape and size of particles. As determined by the analysis of particle shape and size of milled $Ni_{87.3}Fe_{11.3}W_{1.4}$ alloy powders, the shape and size of powder particles depend on milling time. As milling time increases, minimum (Min), maximum (Max) and mean (Mean) particle sizes decrease (Tab. 5).

Tab. V Values of minimum (Min), maximum (Max) and mean (Mean) sizes and the ratio of maximum to minimum(Max/Min) particle sizes of as-deposited and milled $Ni_{87.3}Fe_{11.3}W_{1.4}$ alloy powders obtained at 500 mA cm^{-2}.

Milling time (h)	Min (μm)	Max (μm)	Mean (μm)	Ratio of maximum to minimum size Max/Min
0.0	6.51	741.92	153.01	114.0
4.0	0.98	87.88	13.30	89.7
8.0	0.98	63.45	11.67	64.7
12.0	0.65	34.49	5.6	53.7

The mean particle size of the as-deposited powder is 153.01 μm, and that of powder milled for 12 hours 5.6μm. The maximum particle size of the as-deposited powder is 114 times that of the minimum size. This indicates that powder particles are not spherical in shape. The increase in milling time reduces the ratio of maximum to minimum size. In powders milled for 12 hours, this ratio is only 53.7. Milling causes rounding of powder particles. Fig.s 11 and 12 show cumulative curves for maximum particle size distribution and histograms of the relative frequency of maximum particle size of as-deposited and milled powders.
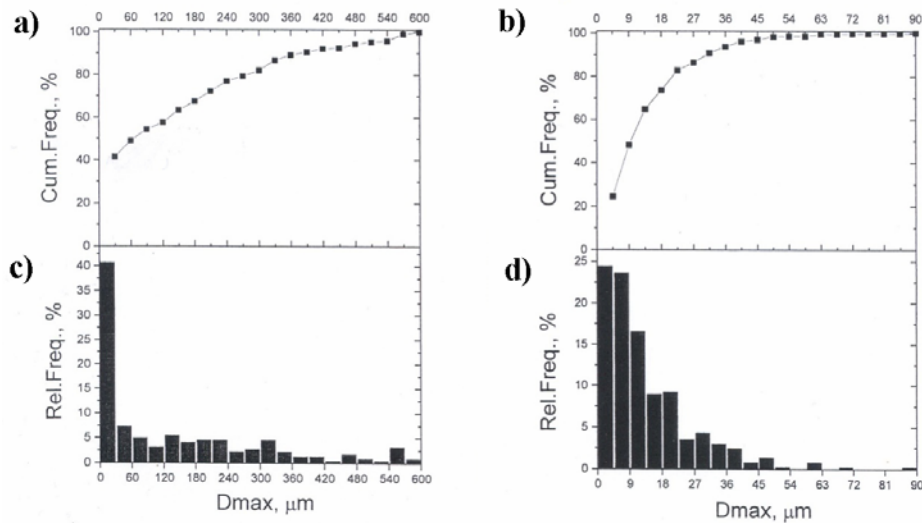
Fig. 11. Cumulative curves for maximum particle size distribution (Dmax): a) as-deposited powder and b) powder milled for 4 hours, and histograms of the distribution of the relative frequency of maximum particle size (Dmax) of: c) as-deposited powder and d) powder milled for 4 hours.
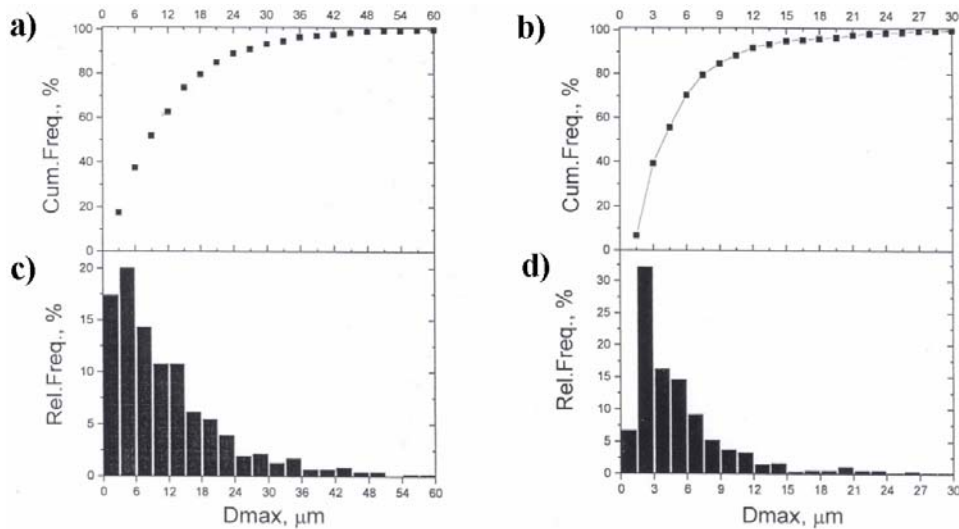
Fig. 12. Cumulative curves for maximum particle size distribution (Dmax) of milled powders: a) 8 hours b) 12 hours, and histograms of the distribution of the relative frequency of maximum particle size (Dmax) of milled powders: c) 8 hours, and d) 12 hours.

The results show that an adequate choice of kinetic and operational parameters of electrodeposition, annealing temperature and milling time can result in nickel-iron-tungsten alloys with predefined chemical compositions, microstructures and morphologies.

4. Conclusion

Nanostructured nickel-iron-tungsten alloys were electrodeposited from an ammonium citrate bath on titanium, copper and mild steel cathodes in the current density range of 50 mA cm^{-2} to 1000 mA cm^{-2}. The cathodic polarization curve was recorded, and the current efficiency of the alloy deposition process was determined. Current efficiency increases with increasing current density up to 600 mAcm^{-2}, and then decreases with further increase in current density. Partial polarization curves for the hydrogen evolution and alloy deposition reactions were determined. At potentials more positive than -960 mV, hydrogen is evolved through the reduction of NH_4^+ and $(HCit)^{3-}$ ions, and at potentials more negative than -960mV the dominant reaction is hydrogen evolution through water reduction. At current densities higher than 300 mAcm^{-2}, alloy deposition is controlled by the diffusion of citrate-ammonium complexes of nickel, iron and tungstate ions. Iron and tungsten contents in the alloy increase, and nickel content decreases with increasing current density from 50 mA cm^{-2} to 300 mA cm^{-2}. At higher current densities, the chemical composition of the alloy is not dependent on current density since electrodeposition is a diffusion-controlled process. As identified by XRD analysis, the electrodeposited alloy is composed of nanocrystals of the FCC-structured solid solution of tungsten and iron in nickel embedded in an amorphous matrix. Increasing the deposition current density and tungsten content in the alloy leads to an increase in amorphous phase content and a decrease in FCC-phase crystal content and size, while simultaneously increasing internal microstrain and minimum density of chaotically distributed dislocations. The nature of the cathode material and solution temperature in the temperature range between 50 ºC and 70 ºC do not have a significant effect on the chemical composition and phase structure of the electrodeposits. The morphology of nickel-iron-tungsten alloy electrodeposits is dependent on the chemical composition and temperature of the solution, deposition current density and the nature of the cathode. Deposition at current densities between 40 mA cm^{-2} and 300 mA cm^{-2} results in the formation of coatings. The coatings having a higher tungsten content (11 wt.%) are much darker and rougher, and have more cracks compared to those with a lower tungsten content ($\leq$ 1.4 wt.% W). As the deposition current increases, roughness and the number of cracks and craters increase as well. The coatings on steel exhibit lower roughness and fewer cracks and craters compared to those on copper and titanium. The deposits with a low tungsten content (1.4 wt.%W) formed in the current density range 500 mA cm^{-2} to 1000 mA cm^{-2} are sponge-shaped, and those with a high tungsten content are powder-like. Large-sized powder particles are cauliflower-shaped and small-sized particles are dendritic.

Annealing the as-produced deposits at t $\geq$ 500 ºC results in amorphous phase crystallization and FCC-phase crystal grain growth in the alloy, accompanied by a decrease in internal microstrain and minimum density of chaotically distributed dislocations. Milling the spongy deposit that contains 1.4 wt.% W also causes amorphous phase crystallization and FCC-phase crystal grain growth. The size and shape of powder particles are dependent on milling time. As milling time increases, the mean particle size and the ratio of minimum to maximum particle size decrease.

Acknowledgments

5. References

1. H.Steerb and H.Warlimont, Rapidly Quenched Metals, Elsevier, Amsterdam,1985.
2. M.Donten, H.Cesiulis, and Z.Stojek, Electrochim. Acta, 45 (2000) 3389.
3. K.R.Sriraman, S.G. Raman, and S.K. Seshadri, Mater. Sci. Eng. A, 418 (2006) 303.
4. K.R.Sriraman, S.G. Raman, and S.K. Seshadri, Mater. Sci. Technol., 22 (2006) 14.
5. F.He, J.Yang, T.Lei, and C.Gu, Appl. Surf. Sci, 253 (2007) 7591.
6. P. Esther, C.JosephKennady, P.Saravanan, and T.Venkatachalam, J. Non-Oxide Glasses, 1 (2009) 301.
7. M. Banerjee, A. Singh, A.K. Majumdar, and A. K. Nigam, J. Phys.: Condens. Matter., 23 (2011) 3060004.
8. L. Ribić-Zelenović, N. Ćirović, M. Spasojević, N. Mitrović, A. Maričić, and V. Pavlović, Mater. Chem. Phys., 135 (2012) 212.
9. M. Spasojević, L. Ribić-Zelenović, N. Ćirović, P. Spasojević, and A. Maričić, Sci. Sinter., 44 (2012) 197.
10. M. Spasojević, N. Ćirović, L. Ribić-Zelenović, P. Spasojević, and A. Maričić, J. Electrochem. Soc. 161(10) (2014) D1-D7.
11. Z. Vuković, P. Spasojević, M. Plazinić, J. Živanić, M. Spasojević. J. Optoelectron. Adv. Mater., 16 (2014) 985
12. S. J. Mun, M.S. Kim, T. H. Yim, J. H. Lee, and T. Kang, J. Electrochem. Soc., 157 (2010) D177.
13. V. B. Singh, Surf. Technol., 7 (1978) 443.
14. L. Ribić-Zelenović, M. Spasojević, and A. Maričić, Mater. Chem. Phys., 115 (2009) 347.
15. L. Ribić-Zelenović, M. Spasojević, A. Maričić, M. Ristić, Sci. Sinter., 41 (2009) 175.
16. L. D. Rafailović, C. Gammer, C. Rentengerger, P. Angerer, and H. P. Karnthaler, J. Alloy. Compd., 543 (2012) 167.
17. M. Spasojević, L. Ribić-Zelenović, and A. Maričić, Sci. Sinter., 43 (2011) 313.
18. E. J. Podlaha and D. Landolt, J. Electrochem. Soc., 143 (1996) 893.
19. A. Maričić, M. Spasojević, L. Rafailović, V. Milovanović, and L. Ribić-Zelenović, Mater. Sci. Forum, 453 (2004) 411.
20. L. Ribić-Zelenović, L. Rafailović, M. Spasojević, and A. Maričić, Phys. B, 403 (2008) 2148.
21. E. Chassaing, K. Vu Quang, and R. Wiart, J. Appl. Electrochem, 19 (1989) 839.
22. O. Younes and E. Gileadi, Electrochem. Solid State Lett., 3 (2000) 543.
23. O. Younes, L. Zhu, Y. Rosenberg, Y. Shacham-Diamond, and E. Gileadi, Langmuir, 17 (2001) 8270.
24. M. Obradović, R.Stevnović, and A. Despić, J. Electroanal. Chem., 552 (2003) 185.
25. M.L. Holt, L.E. Vaaler, J. Electrochem. Soc. 94 (1948) 50.
26. J.Ahmad, K. Asami, A. Takeuchi, D.V. Louzguine, A. Inoue, Mater. Trans. 44 (2003) 1942.
27. N. Mitrović, J. Magn. Magn. Mater., 262 (2003) 302.
28. L. Ribić-Zelenović, L. Rafailović, A. Maričić, and M. Spasojević, J. Optoel. Adv. Mater., 9 (2007) 2681.
29. M. Donten, J. Solid State Electrochem., 3 (1999) 87.
30. W. C. Proud, E. Gomez, E. Sarret, E. Valles, C. Müller, J. Appl. Electrochem. 25 (1995) 770.
31. T. Yamaski, Scripta Mater., 44 (2001) 1497.
32. T. Yamasaki, P. Schlo, K. Ehrlich, Y. Ogino, Nanostruct. Mater., 10 (1998) 375.

Садржај: *Кинетички и оперативни параметри електролизе детерминишу поларизационе карактеристике и искоришћење струје електродепозиције, морфологију, хемијски састав и микроструктуру депозита легуре никла, гвожђа и волфрама. Електродеповане легуре на густинама струје од 50 до 1000 тАст$^{-2}$ се састоје од аморфне фазе и нанокристала FCC фазе чврстог раствора гвожђа и волфрама у никлу. Током одгревања на температурама вишим од 500°C у легури се одвија кристализација аморфне фазе, раст кристалних зрна FCC фазе, смањење унутрашњих микронапрезања и минималне густине хаотично распоређених дислокација. Млевење сунђерастог депозита легуре узрокује кристализацију аморфне фазе, раст кристалних зрна FCC фазе и смањење и заобљење честица праха.*

Кључне речи: *наноструктурна легура, FCC фаза, електрохемијско таложење, млевење, одгревање*